



Mapping of sea ice concentration using the NASA NIMBUS 5 ESMR microwave radiometer data 1972-1977

Wiebke Margitta Kolbe^{1,2}, Rasmus T. Tonboe¹, and Julienne Stroeve^{3,4,5}

¹National Space Institute, Technical University of Denmark (DTU Space), DK-2800 Lyngby, Denmark

²Danish Meteorological Institute (DMI), Copenhagen, Denmark

³University of Manitoba, Winnipeg, Canada

⁴University College London (UCL), London, UK

⁵University Colorado, National Snow and Ice Data Center (NSIDC), Boulder, Colorado, USA

Correspondence: W. M. Kolbe (wmako@space.dtu.dk)

Abstract. The Electrically Scanning Microwave Radiometer (ESMR) instrument on board the NIMBUS 5 satellite was a one channel microwave radiometer measuring the 19.35 GHz horizontally polarised brightness temperature (T_B) from Dec. 11, 1972 to May. 16. 1977. The original tape archive data in swath projection have recently been made available online by NASA Goddard Earth Sciences Data and Information Services Center (GES DISC). Even though ESMR was a predecessor of modern multi frequency radiometers, there are still parts of modern processing methodology which can be applied to the data to derive the sea ice extent globally.

Here we have reprocessed the entire data set using a modern processing methodology, that includes implementation of pre-processing filtering, dynamical tie-points, and a radiative transfer model (RTM) together with numerical weather prediction (NWP) for atmospheric correction. We present the one channel sea ice concentration (SIC) algorithm and the model for computing temporally and spatially varying SIC uncertainty estimates. Post-processing steps include re-sampling to daily grids, land-spill-over correction, application of climatological masks, setting of processing flags and estimation of sea ice extent, monthly means and estimation of trends. This sea ice dataset derived from NIMBUS 5 ESMR extends the sea ice record with an important reference from the mid 1970s. To make a consistent analysis of the sea ice development through time easier, the same grid and landmask as for EUMETSAT's OSI-SAF SMMR based sea ice CDR have been used for our ESMR dataset. SIC uncertainties have been included for further ease of comparison to other datasets and time periods.

We find that our sea ice extent in the Arctic and Antarctic in the 1970s is generally higher than those available from the National Snow and Ice Data Center (NSIDC) Distributed Active Archive Center (DAAC) derived from the same ESMR dataset, with mean differences of 240.000 and 590.000 km², respectively. The largest differences reach up to 2 million km², when comparing monthly sea ice extents. Such large differences cannot be explained by the different grids and landmasks of the datasets alone, and must therefore also result from the difference in data filtering and algorithms, such as the dynamical tie-points and atmospheric correction.

The new ESMR SIC data set has been released as part of the ESA Climate Change Initiative Programme (ESA CCI) and is publicly available at: <http://dx.doi.org/10.5285/34a15b96f1134d9e95b9e486d74e49cf> (Tonboe et al., 2023).



1 Introduction

25 Arctic sea ice extent (SIE) in September has been decreasing at a rate of about 12 percent per decade since the launch of
modern satellite multi-frequency microwave radiometers in 1978 (Comiso et al., 1980; Tonboe et al., 2016; Onarheim et al.,
2018; Stroeve and Notz, 2018; Lavergne et al., 2019). This negative sea ice trend in the Northern Hemisphere already started
in the 1970s (Rayner et al., 2003; Walsh et al., 2017), though regional trends can differ, as seen for example within the Barents
Sea (Chapman and Walsh, 1991). In the Antarctic there are large regional differences in SIE trends but until recently, the
30 overall trend was positive due to sea ice dynamics (Turner et al., 2009; Sun and Eisenman, 2021). This has changed however
in the last decade as a result of several record lows, and as such overall trends have shifted to a more homogeneous pattern,
(Schroeter et al., 2023), and in summer (NDJF) the overall trends are now slightly negative. Until recently, the slightly positive
trend was believed to be part of long term natural variability that overshadowed the effects of global warming starting in the
1960s (Wang et al., 2019; Stammerjohn et al., 2008; Thompson and Solomon, 2002; Ferreira et al., 2015; Singh et al., 2019;
35 Fogt et al., 2022). In order to fully understand the drivers of sea ice variability, extending the sea ice data record backwards in
time is essential.

Globally, SIE information prior to the satellite data record was largely from ice charts and ship observations. While there have
been efforts to include this data in long-term assessments of sea ice change, the data are typically provided in relatively coarse
spatial and temporal resolution (1 deg grid) (Walsh et al., 2019) interpolating in both time and space (Titchner and Rayner,
40 2014). Only satellite based data-sets offer the ability to cover both hemispheres at improved spatial and temporal resolutions,
and generally have consistency in processing methods (Lavergne et al., 2019). Sea ice concentration (SIC) derived from Nimbus
5 Electrically Scanning Microwave Radiometer (ESMR) data was previously processed by Parkinson et al., 2004. Here we
apply a new processing method that is comparable to the EUMETSAT/ESA CCI SIC record from 1978 and on-wards (see
Andersen et al., 2006; Tonboe et al., 2016). This method reduces atmospheric noise regionally over both ice and water surfaces
45 and uses the pre-processed data to develop a SIC algorithm calibration that is effective in removing both instrument drift and
offsets. Seasonal sea ice signature variations are removed by using dynamical tie-points. Lastly, the algorithm calculates time
and spatially varying uncertainty estimates. The ESMR SIC data are presented on the same grid and with the same masking as
the EUMETSAT/ESA CCI record, which makes these two records directly comparable. This and the modern processing chain
mentioned above warrant the reprocessing presented in this article.

50 In the following Section 2, the satellite and reanalysis data are described, including the formatting and initial filtering of
the data. Section 3 describes the radiative transfer model (RTM) used for the atmospheric correction, the dynamical tie-points,
the SIC algorithm with uncertainty estimations, the land-spill-over method and data flags assigned during post-processing. In
Section 4, the resulting SIC dataset is presented and compared to other datasets. Finally, Section 5 consists of a discussion and
Section 6 provides the conclusions of this work.



55 2 The NIMBUS 5 ESMR instrument and data

The NIMBUS 5 ESMR instrument was a cross-track scanner measuring at 78 scan positions perpendicular to the flight track with a maximum incidence angle of about 64 degrees to both sides. No direct observations at nadir have been made, the closest positions being at +/- 0.7 degrees. The near circular orbit height was about 1112 km with an inclination of 81 degrees. The phased array antenna dimensions was 85.5 x 83.3 cm and the spatial resolution about 25 km near nadir increasing to about 160 x 45 km at the edges of the swath. The full swath was about 3100 km with varying incidence angle and spatial resolution giving a very good (unprecedented) daily coverage in polar regions with no gaps, i.e. no pole holes. The ESMR onboard the NIMBUS 5 satellite was a one channel 19.35 GHz horizontally polarised microwave radiometer operating from 11. December 1972 until 16. May 1977 (1617 days) with some interruptions (see list of days with missing files in Appendix A2). Due to a hot-load anomaly, there are major data gaps between March to May and again in August 1973. Another major data gap occurred from 3 June 1975 until 14 September 1975 because the ground segment was used for receiving Nimbus 6 data instead. When resuming operation in September 1975 the instrument was only operated approximately every other day. From late 1976 to the end of the mission, operation was highly irregular. The last file in the data-set is from 16 May 1977. The data have recently been made available online by NASA in the original tape archive format (TAP-files).

2.1 Formatting and co-location of brightness temperatures and ECMWF ERA5 data

70 The ESMR data were retrieved from the NASA Goddard Earth Sciences Data and information services center (GES DISC) on-line data archive (NASA GSFC, 2016). This data set contains, along with a number of instrument and geographical parameters, 19.35 GHz calibrated brightness temperatures expressed in units of Kelvin. The raw data was recovered by NASA from the magnetic tapes, called Calibrated Brightness Temperature Tapes (CBTT), where they were stored in the original binary TAP file format, each file corresponding to a particular orbit (NASA GSFC, 2016).

75 All variables in the TAP files were read using online NASA software and converted to NetCDF format without changing the original data structure. Each data point in the TAP file was matched with European Centre for Medium Range Weather Forecast (ECMWF) ERA5 re-analysis data (Hersbach et al., 2020) in time and space (nearest) and appended to a NetCDF file, serving as input to the processing chain. The resulting data are structured in arrays line by line (across-track). Appendix A1 summarizes the variables included in the NetCDF files.

80 2.2 Initial filtering and correction of brightness temperatures

NASA provides a correction on the brightness temperature data to account for lobe structure, antenna loss and angular T_B variation NASA CR, 1974. According to NASA the correction was needed because: “The cause of the gross variations in antenna properties which were observed soon after launch has been determined to be a cross-polarized grating lobe [...] The problem does not exist for the near-nadir beam positions so these positions are unaffected. [...] An empirical calibration has been developed which removes the effect of the lobe structure and antenna loss, which vary with position, and roughly corrects for angular variations in viewing geometry.” (NASA CR, 1974, p.400).



Originally, it was planned to use only lobe corrected T_{BS} with their natural angular dependency, but we did not find a way to extract this in the NASA provided data-set. Essentially, only the combined lobe and angular correction, which is a function of brightness temperature, can be removed altogether from the data NASA provides. Thus, the T_{BS} do not vary as a function of incidence angle, as would be expected for T_{BS} from the sea surface and sea ice.

Despite the corrections done by NASA, the ESMR data still contain erroneous T_{BS} , scan-lines, sudden jumps in the calibration and other obvious artifacts.

Since the ESMR data contains corrupted data and erroneous scan-lines, filtering is needed before the data can be used for sea ice mapping. The filters that we apply are described in Eqns 1-4. They are applied in the same order as described here and if only a single data point or a couple of scan lines are affected only these data points and scan lines are removed from the file. If the whole file is corrupted then it is deleted.

The first filter, the analog filter, which is used for filtering erroneous T_{BS} and scanlines, is based on the 16 analog voltage entries in the data. The users guide does not explain very well what the 16 entries really are but jumps in these analog signals correspond to anomalous T_{BS} . Our analog filter computes the absolute gradient in the analog signals and anything over a value of 10 is removed. This threshold was estimated experimentally.

The following set of filters are applied using the processed T_B (in Kelvin) from the previous step. The filters are applied in the following order:

The second filter in Eq. 1 removes data that are non-physical and outside the expected range for sea and ice surfaces.

$$90K < T_B \leq 273.15K \quad (1)$$

For all data points that lie inside the range specified in Eq. 1, the third filter in Eq. 2 removes erroneous scan-lines (across track rows). The threshold of 50K was estimated experimentally:

$$\frac{\sum_j^n |T_{B_{j,i+1}} - T_{B_{j,i}}|}{n} > 50K \quad (2)$$

where T_{B_i} in Eq. 2 is an across track row of T_B and i is an index along track, while j is an index across track.

The fourth filter in Eq. 3 removes single T_B outliers:

$$|p_i - p_{i-1}| + |p_{i+1} - p_i| \geq 150K \quad (3)$$

where p is a single pixel T_B and i is an along track index. The fifth filter in Eq. 4 removes neighbouring T_{BS} which are locked on the same value.

$$|p_{i+6} - p_{i+5}| + |p_{i+5} - p_{i+4}| + |p_{i+4} - p_{i+3}| + |p_{i+3} - p_{i+2}| + |p_{i+2} - p_{i+1}| + |p_{i+1} - p_i| \neq 0 \quad (4)$$

The outer data points of the swath edges showed significant higher noise levels and coarser resolution than the near nadir data points (Veng, 2021). Therefore, after the filtering we additionally remove the 4 outermost data points of the swath, corresponding to incidence angles between 57 and 64 degrees on both sides. The new outer edges of the swath data is then at ~ 56



degrees, similar to modern microwave radiometers for sea ice retrieval of 50-55 degrees (AMSR (Meisner and Wentz, 2000), SMMR (Wentz, 1983), SSM/I (Wentz, 1997)).

Before the filtering, the dataset contained 13496 orbital data files; after filtering there are 10649 (~79%) good files left. A complete list of days where data are missing after filtering and no SIC could be retrieved is given in appendix A3.

3 The radiative transfer model

The Radiative Transfer Model (RTM) has been developed specifically for atmospheric noise reduction and it is comparable to the RTM's used in Andersen et al., 2006 and Tonboe et al., 2016 but with the addition that this ESMR RTM (Eq. 5) can be applied for different incidence angles over both ocean and ice. The RTM takes as input: atmospheric columnar water vapor V [mm or kgm^{-2}], 10 m wind speed W [ms^{-1}], atmospheric columnar cloud liquid water L [mm or kgm^{-2}], sea surface temperature T_s [K], ice emitting layer temperature T_i [K], sea ice concentration c_{ice} [0-1], and incidence angle [deg]. In return, it simulates the top-of-the-atmosphere 19.35 GHz T_B at horizontal polarisation.

$$T_B = RTM(V, W, L, T_s, T_i, c_{ice}, \theta) \quad (5)$$

The RTM uses the atmospheric part of the model described in Wentz, 1997 to compute atmospheric emission, transmissivity and reflectivity at the sea surface (open water) together with added modules for simulating the sea ice emissivity (Fig. 1) and open water reflectivity as a function of incidence angle.

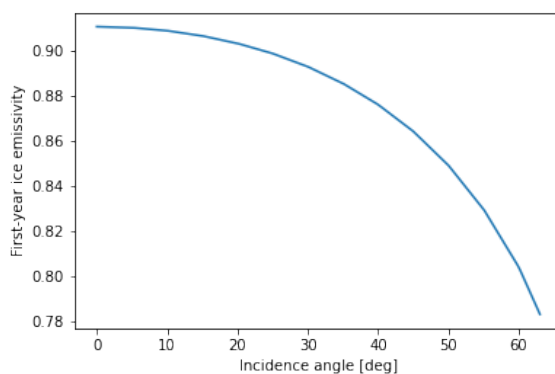


Figure 1. The first year-ice emissivity used in the RTM

For the sea ice emissivity, a look-up-table is produced from a simulation using a combined sea ice thermodynamic and emission model during Arctic winter on first-year ice. The thermodynamical and emission model set-up and the simulations are described in Tonboe, 2010. The emissivities as a function of incidence angle are shown in Figure 1 and the look-up-table is given in Table 1.



Incidence angle, θ , and first-year ice emissivity, E_{ice}														
θ	0	5	10	15	20	25	30	35	40	45	50	55	60	65
E_{ice}	0.91	0.91	0.91	0.91	0.90	0.90	0.89	0.89	0.88	0.86	0.85	0.83	0.80	0.77

Table 1. Sea ice emissivity look-up-table.

Sea water permittivity, which is used to estimate the calm sea reflectivity (Eq. 6) as a function of temperature, is computed using equation E64 (p. 2046) in Ulaby et al., 1986. The permittivity is almost invariant of the water salinity at 19 GHz and a constant value of 34 ppt is used here.

The calm sea (Fresnel) power reflection coefficient, r_h , as a function of the relative permittivity, ϵ , and the incidence angle, θ , for a lossy medium, is computed using Eq. 1.52 in Schanda, 1986, i.e.

$$r_h(\theta) = \frac{(p - \cos(\theta))^2 + q^2}{(p + \cos(\theta))^2 + q^2}, \quad (6)$$

where

$$p = \frac{1}{\sqrt{2}} ((\epsilon'_r - \sin^2\theta)^2 + \epsilon''_r{}^2)^{\frac{1}{2}} + (\epsilon'_r - \sin^2\theta) \quad (7)$$

and

$$q = \frac{1}{\sqrt{2}} ((\epsilon'_r - \sin^2\theta)^2 + \epsilon''_r{}^2)^{\frac{1}{2}} - (\epsilon'_r - \sin^2\theta) \quad (8)$$

where the relative permittivity $\epsilon_r = \epsilon'_r + \epsilon''_r j$ of the water surface is a complex number. The calm sea emissivity, E_0 , is then

$$E_0 = 1 - r_h. \quad (9)$$

The rough water surface emissivity component, E_W , is added to the calm sea emissivity, E_0 , to produce the total sea water emissivity, E_{water} . Between ESMR incidence angles of 0 and 63 degrees the 19.35 GHz horizontal polarization E_W sensitivity to wind speed is an almost a linear function ($\frac{\Delta(E_W T_s)}{\Delta W} = 0.0094\theta + 0.3$) of incidence angle, θ , (Meisner and Wentz, 2012), i.e.

$$E_W = \frac{W(0.0094\theta + 0.3)}{T_s}, \quad (10)$$

and

$$E_{water} = E_0 + E_W \quad (11)$$

where θ is the incidence angle in degrees, W is the wind speed, and T_s is the sea surface temperature [K].

This combination of E_0 and E_W follows the procedure described in Wentz, 1997.



The resulting brightness temperature is a linear combination of the sea water and sea ice emission weighted by the SIC
160 following Andersen et al., 2006.

$$T_B = T_{BU} + \tau((1 - c_{ice})E_{water}T_s + (1 - c_{ice})(1 - E_{water})(\Omega T_{BD} + \tau T_{BC}) + c_{ice}E_{ice}T_i + c_{ice}(1 - E_{ice})(T_{BD} + \tau T_{BC})) \quad (12)$$

where T_{BU} is the up-welling brightness temperature from the atmosphere, τ the atmospheric transmissivity, E_{water} the
water surface emissivity, E_{ice} the sea ice emissivity, Ω the reflection reduction factor due to water surface roughness, T_{BD} the
down-welling brightness temperature, and T_{BC} the cosmic background brightness temperature (2.7 K).

165 EMSR-simulated T_B s and emissivities have been compared with other simulated T_B s using other RTMs for AMSR (Meisner
and Wentz, 2000), SMMR (Wentz, 1983), SSM/I (Wentz, 1997) for a constant incidence angle of 55 degrees, which is close
to the incidence angle of the other instruments and RTMs (53-55 degrees). The comparison showed that the T_B s of the EMSR
RTM are within the same range (approx. 2K) of values of the other models and therefore it seems to be reasonable given the
differences in instruments centre frequency and measurement geometry. It is noted that in the correction procedure, differences
170 between two simulated T_B s are used to minimize model biases. Even if the absolute values of the RTM simulated T_B s are
biased, this bias would be removed by taking the difference between two simulated T_B s, which is the only part used in the
correction.

3.1 Tie-points and geophysical noise reduction

Tie-points are typical signatures of 100 % ice and open water (0 % ice) and are used in SIC algorithms as a reference for
175 estimating the total ice fraction per satellite pixel c_{ice} . Using dynamical tie-points aims to reduce SIC biases that may result
from seasonal and inter annual variations of T_B s (Kongoli et al., 2011), instrument drift and RTM and ERA5 biases. For
example, Comiso and Zwally, 1980 argue that the variations in average open water T_B s near the ice edge are affected primarily
by variations in instrument calibration, and they describe the drop followed by a sharp increase seen in Figure 2 in 1975 as an
instrument drift issue.

180 Our EMSR tie-points are derived on a daily basis from the swath files. Regions of open water and high SICs are selected
for each hemisphere, resulting in two regions of sea ice and two of open water for both hemispheres. The selection of the
four tie-points is based on criteria set for SIC from ERA5, distance from ice edge, observed brightness temperature, latitude
and sea surface temperature, shown in table 2. While computed daily, these are subsequently combined into 15-day running
mean tie-points, 7 days ahead and 7 days behind the processed date shown in Figure 2. The 15-day averaging period has been
185 maintained even at the beginning and end of the data-set and when there are data gaps.



	Ice	Ocean
Arctic	$90 > \text{latitude} > 32$ sea ice concentration (ERA5) > 0.8 mean sea ice concentration (ERA5) of a 5×5 grid point box > 0.8 $100 \text{ K} < \text{brightness temperature} < 274 \text{ K}$	$90 > \text{latitude} > 32$ sea ice concentration (ERA5) = 0 mean sea ice concentration (ERA5) of a 5×5 grid point box < 0.01 sea surface temperature (ERA5) $> 278 \text{ K}$ $90 \text{ K} < \text{brightness temperature} < 180 \text{ K}$
Antarctic	$-90 < \text{latitude} < -48$ sea ice concentration (ERA5) > 0.8 mean sea ice concentration (ERA5) of a 5×5 grid point box > 0.8 $100 \text{ K} < \text{brightness temperature} < 274 \text{ K}$	$-90 < \text{latitude} < -48$ sea ice concentration (ERA5) = 0 mean sea ice concentration (ERA5) of a 5×5 grid point box < 0.01 sea surface temperature (ERA5) $> 278 \text{ K}$ $90 \text{ K} < \text{brightness temperature} < 180 \text{ K}$

Table 2. Criteria for the four different tie-points.

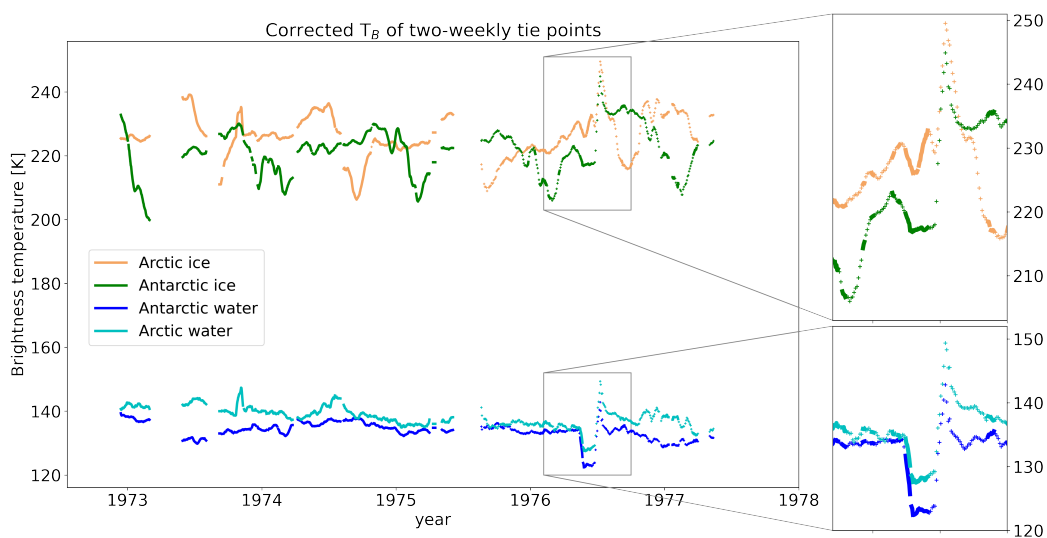


Figure 2. The two-weekly tie-points for Arctic and Antarctic ice and water after T_B correction. The boxes are showing the period during May-July 1976 with obvious instrument calibration issues.

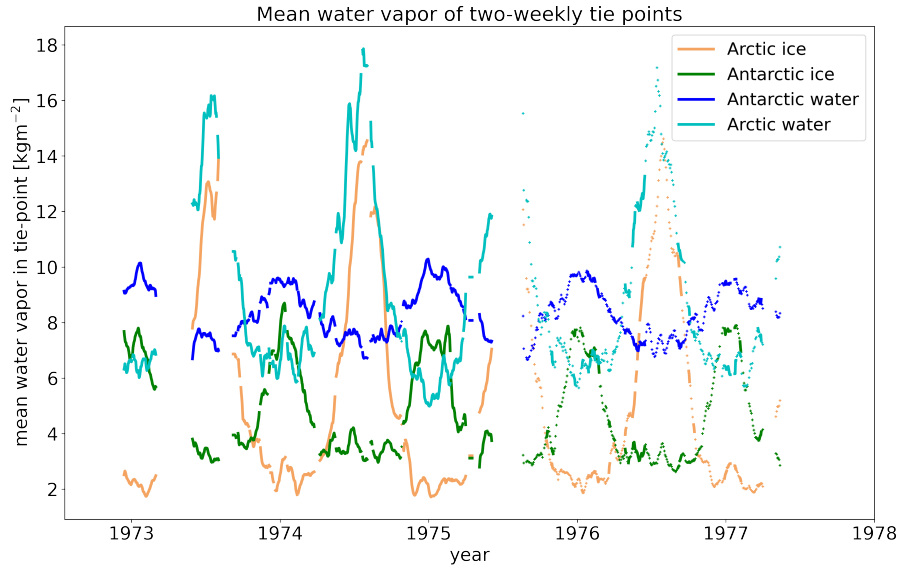


Figure 3. Mean Atmospheric water vapor for all grid points included in the four tie-points

The per grid-point T_B correction term $\Delta T_{B,simulated}$, is the difference between a simulated reference T_B using mean values of total column water vapor [kg/m^2] in the atmosphere (\bar{V}), 10 m wind speed [m/s] (\bar{W}), total column cloud liquid water [kg/m^2] in the atmosphere (\bar{L}), the sea surface temperature (\bar{T}_s), the ice emitting layer temperature (\bar{T}_i) as input to the RTM and a simulated T_B using the actual ERA5 values (V, W, \bar{L}, T_s, T_i) for the grid-point. The T_B is not corrected for cloud liquid
 190 water, L , so the mean L is input to both the reference and the actual simulation. $\Delta T_{B,simulated}$ can both be negative and positive and after correction, the T_B s have reduced sensitivity to the geophysical noise sources: V, W, T_s, T_i . The fact that the correction term is the difference between two RTM simulations minimizes the impact of biases in the model and the ERA5 data.

The correction term is added to the measured T_B , i.e.

$$195 \quad T_{B,corrected} = T_{B,measured} + \Delta T_{B,simulated}, \quad (13)$$

where

$$\Delta T_{B,simulated} = RTM(\bar{V}, \bar{W}, \bar{L}, \bar{T}_s, \bar{T}_i, c_{ice}, \theta) - RTM(V, W, \bar{L}, T_s, T_i, c_{ice}, \theta) \quad (14)$$

where $c_{ice} = 0$ is the open water tie-point and $c_{ice} = 1$ the ice tie-point. Following (Svendsen et al., 1983), T_i is computed as:

$$T_i = 0.4 \cdot T_{2m} + 0.6 \cdot 272, \quad (15)$$



200 where T_{2m} is the 2 m air temperature. The horizontal bars above the variable indicate that they are daily mean values for cluster of points selected for the tie-point. The mean water vapor, V in the tie-point is shown in Figure 3.

Figures 4 and 5 show the correction term, $\Delta T_{B,simulated}$, Jan. 1., 1974 over open water in the Northern and Southern Hemisphere respectively. The path-length through the atmosphere is longest at high incidence angles and shortest near nadir, and thus, the absolute value of the correction is largest at high incidence angles. For example, when the atmosphere is driest in
 205 the reference compared to the actual simulation, the ends of the corrected T_B turn negative, while they turn strongly positive when the reverse is true.

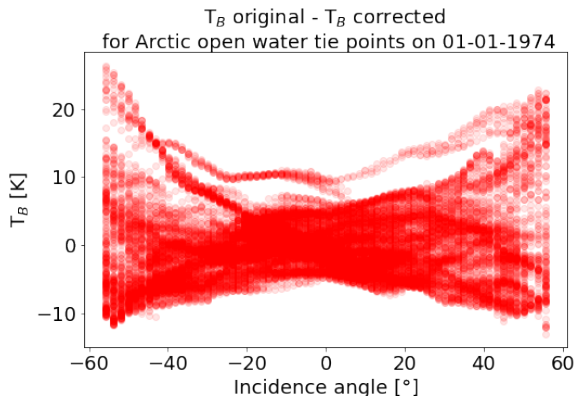


Figure 4. Difference of T_B s, before and after correction with a mean reference, Northern Hemisphere, open water tiepoints

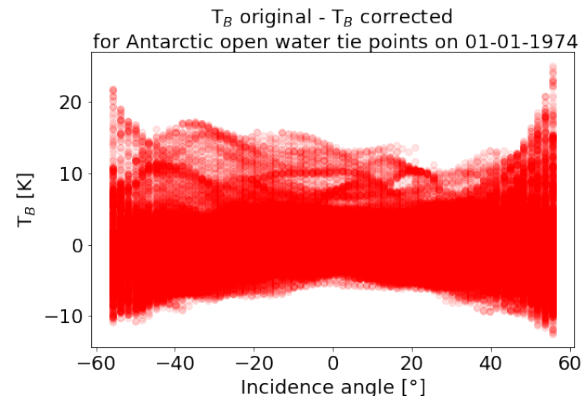


Figure 5. Difference of T_B s, before and after correction with a mean reference, Southern Hemisphere, open water tiepoints

The correction works best over open water areas, where it acts as only an atmospheric correction. The RTM appears to better simulate the relevant emission processes in the atmosphere, and the ERA5 data more accurately quantifies the atmospheric noise sources. Over sea ice, geophysical noise sources are related to processes in the snow and ice profile (Tonboe et al., 2021)
 210 which are not characterised by the RTM except for the emitting layer temperature T_i . The T_i , which is used as input to the RTM, is estimated from the 2 meter air temperature in the ERA5 data using Eq. 15. This is important because ESMR is a single channel instrument and thus the T_B and also the derived c_{ice} are sensitive to emitting layer temperature.

The standard deviation of the brightness temperatures for water points in both hemispheres, before and after the correction, is shown in figures 6 & 7.

215 3.2 The sea ice concentration (SIC) and its uncertainty

SIC (c_{ice}) is estimated using the measured brightness temperature ($T_{B,measured}$) and the open water ($T_{p,water}$) and ice ($T_{p,ice}$) tie points, i.e.

$$c_{ice} = \frac{T_{B,measured} - T_{p,water}}{T_{p,ice} - T_{p,water}} \quad (16)$$

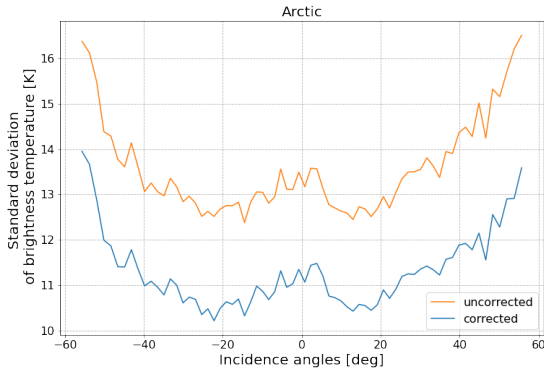


Figure 6. Standard deviations of T_{BS} , before and after correction in the Northern Hemisphere, 1974 January. Only filtered for ocean points with ERA5 SIC and SST.

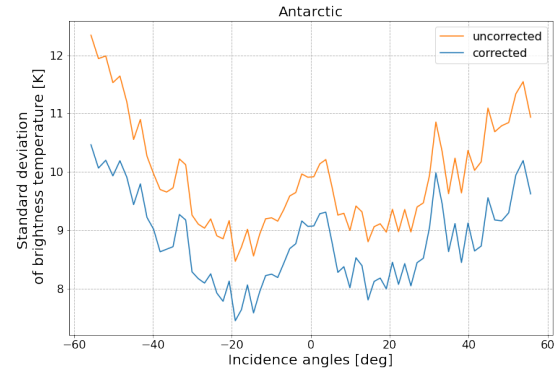


Figure 7. Standard deviations of T_{BS} , before and after correction in the Southern Hemisphere, 1974 January. Only filtered for ocean points with ERA5 SIC and SST.

Because the RTM requires c_{ice} as input, c_{ice} is processed iteratively in two steps: 1) the c_{ice} is first estimated using uncorrected T_{BS} and tie-points derived from uncorrected data. The c_{ice} estimate is truncated to the interval between 0 and 1 and an open water filter is applied, forcing all c_{ice} values less than 0.15 to 0. 2) The c_{ice} estimate from step (1) is used in the RTM calculation (Eq. 5) together with ERA5 data for the geophysical noise reduction of the T_{BS} and c_{ice} is then estimated again in a second iteration, this time using corrected T_{BS} and corrected tie-points. The mean values of \bar{V} , \bar{W} , \bar{L} ... used in the reference simulation is a weighted average with c_{ice} of the mean water and ice tie-point values respectively, i.e. c_{ice} is used as a ratio to mix the two tie-point values to create mean values of the NWP data for any sea ice concentration.

Iterations to update c_{ice} could in principle continue. However, tests show that updates are small after one iteration and we only iterate once (e.g. Lavergne et al., 2019).

The total SIC uncertainty is the combination of two components: 1) algorithm uncertainty, which includes instrument noise and tie-point variability (geophysical noise) and 2) re-sampling uncertainty, which is uncertainty due to data re-sampling.

The algorithm uncertainty is the squared sum of three independent components following Parkinson et al., 1987:

$$\delta c_{ice,algorithm} = \left(\left(\frac{\delta T_B}{T_{p,ice} - T_{p,water}} \right)^2 + \left(\frac{-(1 - c_{ice})\delta T_{p,water}}{T_{p,ice} - T_{p,water}} \right)^2 + \left(\frac{-c_{ice}\delta T_{p,ice}}{T_{p,ice} - T_{p,water}} \right)^2 \right)^{\frac{1}{2}} \quad (17)$$

where the first term in eq. 17 represents variations due to instrument noise, estimated to a δT_B brightness temperature error of 3 K (Parkinson et al., 1987).

Without the instrument noise term, which is already included in the two tie-point uncertainties, the second and third term in eq. 17 are used to compute the algorithm uncertainty, $\delta c_{ice,algorithm}$:

$$\delta c_{ice,algorithm} = \left(\left(\frac{-(1 - c_{ice})\delta T_{p,water}}{T_{p,ice} - T_{p,water}} \right)^2 + \left(\frac{-c_{ice}\delta T_{p,ice}}{T_{p,ice} - T_{p,water}} \right)^2 \right)^{\frac{1}{2}} \quad (18)$$



where $\delta T_{p,water}$, is the water tie-point error, here the (one) standard deviation of the daily tie-point, $\delta T_{p,ice}$, is the ice tie-point error (e.g. one standard deviation of the daily tie-point). The water and ice tie-point errors are weighted by the SIC, and all three errors are normalized with the ice - water brightness temperature contrast and the 2-weekly tie-points. The algorithm uncertainty is computed on swath data.

The re-sampling uncertainty, $\delta c_{ice, re-sampling}$ is the maximum c_{ice} - minimum c_{ice} difference of a 3 x 3 pixel window. The re-sampling uncertainty is computed on re-sampled data (e.g. Lavergne et al., 2019).

The total uncertainty is the squared sum of the algorithm and the re-sampling uncertainty, i.e.

$$\delta c_{ice, total} = (\delta c_{ice, algorithm}^2 + \delta c_{ice, re-sampling}^2)^{\frac{1}{2}} \quad (19)$$

The two uncertainty components and the total uncertainty are included in the data file.

3.3 Land-spill-over correction and post-processing

Land-spill-over correction is following the procedure described in Markus and Cavalieri, 2009. A 5 by 5 pixel neighbourhood of the land mask (EASE2 version 2, by OSI-SAF) is analysed to determine which coastal points should be corrected. The land mask is divided into two classes: land points, which are given a value of 90% SIC and open ocean points. If the difference between the original land mask and the calculated mean mask by the 5 by 5 window is larger than the previously estimated SIC (the RTM corrected & re-sampled SIC), i.e. the SIC is smaller than the theoretical value of the land spill over only, the SIC value is set to 0% and the status flag variable of the data set is raised to 8.

Additionally, a monthly climatology (also by OSI-SAF, same version as land mask) is used to set SIC to 0% and mark open water points by a climatology boundary, which is indicated by a status flag value of 64. Afterwards the land mask is also used to also mark lakes and coastal areas with status flags 2 and 32 respectively. An overview of all status flag values is shown in table 4:

status flag values for SIC retrievals	
no flag/flag 0	Nominal retrieval by the SIC algorithm
flag 1	Land
flag 2	Lake
flag 4	SIC is set to zero by the open water filter
flag 8	SIC value is changed for correcting land spill-over effects
flag 16	Handle with caution, the 2m air temperature is high at this position, and this might be false ice
flag 32	Coast
flag 64	SIC is set to zero since position is outside maximum sea ice climatology
flag 128	Point not accepted but no other flags raised

Table 4. Description of the *status_flag* variable of the dataset.



The results of the post-processing are included in the daily NetCDF files, for the Northern and Southern Hemisphere, respectively. 260

4 Results

A list of all output variables in the daily SIC files and a short description of them can be seen in Appendix A2. Examples of monthly means of the SIC and mean uncertainty can be seen in figures 8-11.

It is worth noticing that the coverage in figure 8 is complete and because of ESMR's wide swath width of 3100 km and its 265 inclination, the North Pole is covered in contrast to the satellite microwave radiometers following NIMBUS 5 ESMR which have a "pole hole". The area covered by multiyear ice in the central Arctic has lower SIC than the first-year ice regions. This is a consequence of the one channel SIC algorithm. In figure 9 and 11 it can be seen that the uncertainties are largest near the ice edges, as expected. This is due to the re-sampling uncertainty which is dominating near the ice edge where T_B spatial variability is high.

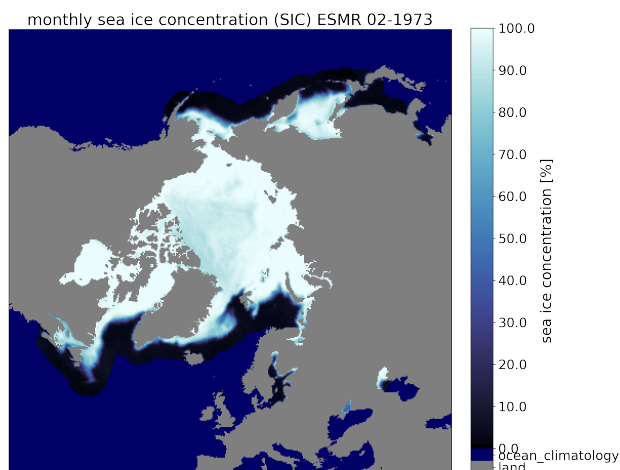


Figure 8. Monthly mean SIC for February 1973, Northern Hemisphere.

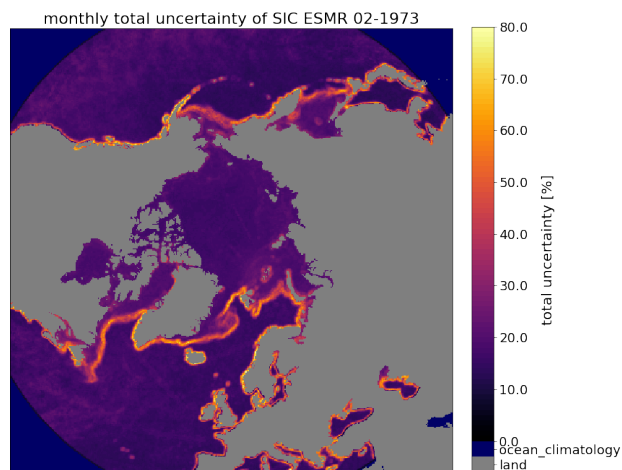


Figure 9. Monthly mean uncertainty for February 1973, Northern Hemisphere. Water areas with no uncertainty due to the ocean climatology are displayed in dark blue.

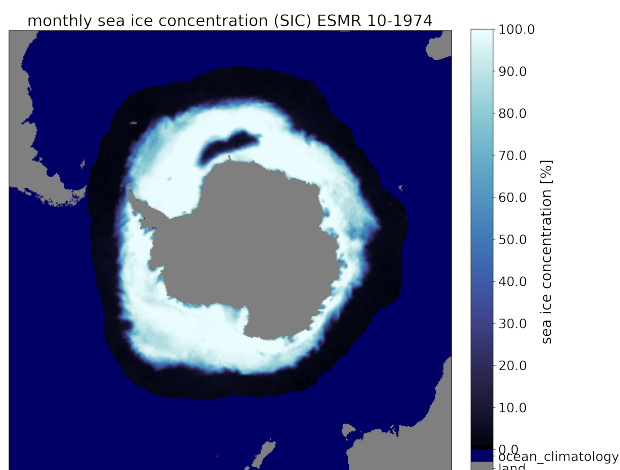


Figure 10. Monthly mean SIC for October 1974, Southern Hemisphere

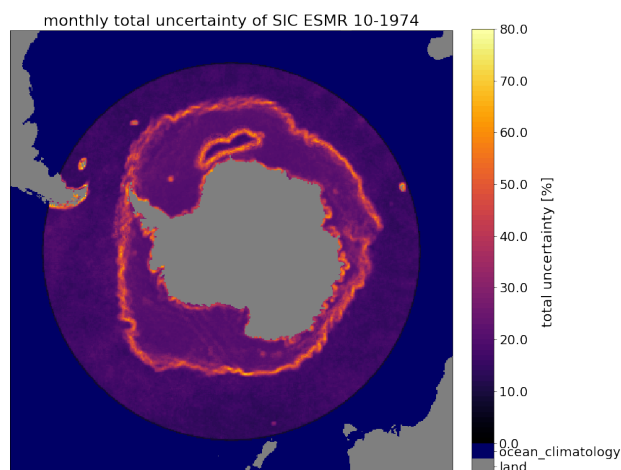


Figure 11. Monthly mean uncertainty for October 1974, Southern Hemisphere. Water areas with no uncertainty due to the ocean climatology are displayed in dark blue.

270 The SIC shows interesting sea ice features in the years 1972-1977. One such feature is the Odden ice tongue extending eastward from the East Greenland Current, visible in figure 8, while another feature is the Maud Rise Polynya, an open water area encircled by sea ice, in the Southern Hemisphere, which can be seen in figure 10. Both examples were much larger in extent in the 1970s and more frequently occurring than they are today (Comiso et al., 2001; Cheon and Gordon, 2019; Jena et al., 2019).

275 The daily coverage of valid data points that passed all filtering varies a lot through the ESMR operating period. While there is nearly full coverage for the first months, it gets much worse after the summer of 1975 when the instrument only recorded data every second day. An example of the poor coverage is shown for May 1976 in figure 12 and 13.

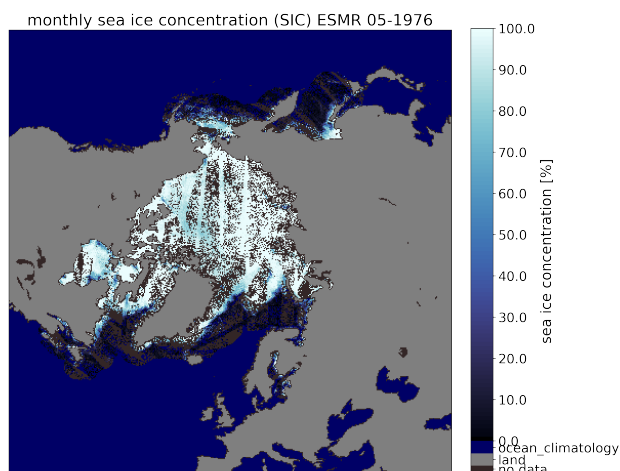


Figure 12. Monthly mean SIC for May 1976, Northern Hemisphere

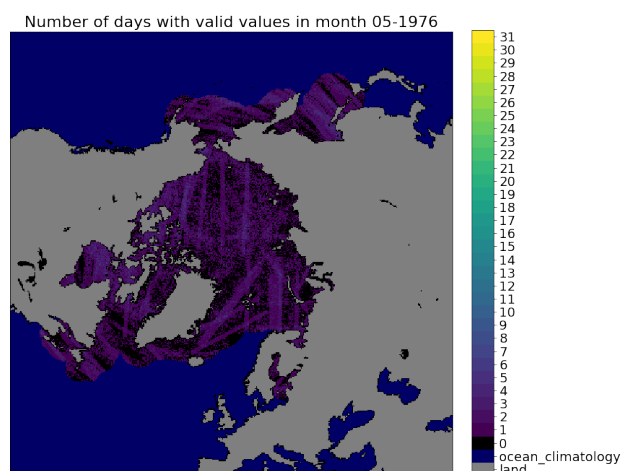


Figure 13. Example of poor monthly coverage for May 1976, Northern Hemisphere. Water areas that would show a full daily coverage due to the ocean climatology are displayed in dark blue, to avoid misleading comparisons. Number of days with valid data are indicated by the colorbar.

Monthly averaged SIC are derived to compare our results against other datasets. Only months with a 99% coverage have been used in the comparison, i.e. 99% of all grid points is at least covered once per month. From the monthly SIC, monthly mean SIE are calculated using a threshold of 30% c_{ice} . In figures 14 & 15 the ESMR data set (orange line) is shown together with the OSI-SAF CDR (blue line) for 1979-2022 (EUMETSAT, 2017a & EUMETSAT, 2017b) and the sea ice extent derived from NSIDC's NIMBUS 5 ESMR ice concentration product (green line) (Parkinson et al., 2004) using the same threshold for all products (30%).

The comparison shows comparable SIE levels around 1980. In general, our ESMR data set has slightly higher monthly SIE values than the NSIDC's ESMR product, even though the seasonal pattern is the same.

The mean difference between our sea ice extent and that from NSIDC is 0.24 mill. km² in the Arctic and 0.59 mill. km² in the Antarctic for the whole data set.

For the Northern Hemisphere the SIE seems to have been slightly lower during the operational period of NIMBUS 5 ESMR 1972 to 1977 than during the operational period of NIMBUS 7 SMMR from 1978 to 1987. In the Southern Hemisphere the



290 values of the second half of the 1970s seem to have been around the same magnitude as the largest SIE during the 2014/2015 season.

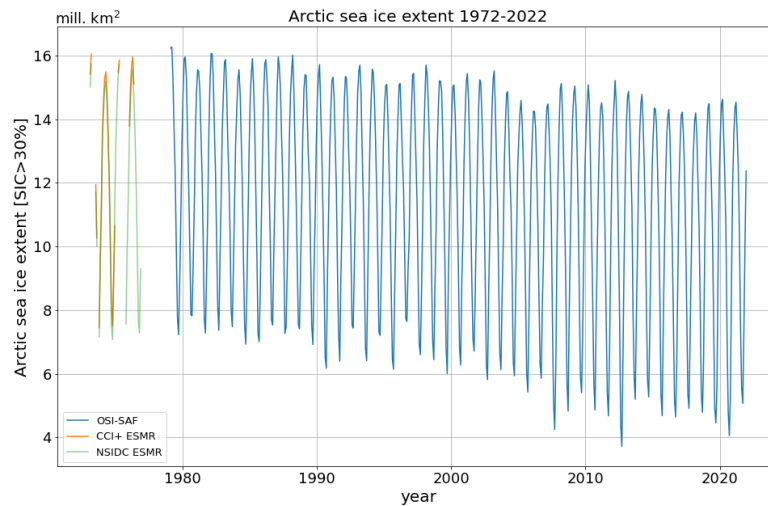


Figure 14. Monthly sea ice extent time series for the Arctic based on a 30% sea ice threshold. The orange curve shows values of the ESMR dataset which have a 99% monthly coverage of the hemisphere, while the blue curve is based on the SIC products by OSI-SAF (EUMETSAT, 2017a & EUMETSAT, 2017b), where the 30% threshold has been applied as at: EUMETSAT, 2017c. The green line represents NSIDC's ESMR SIC product. (Parkinson et al., 2004).

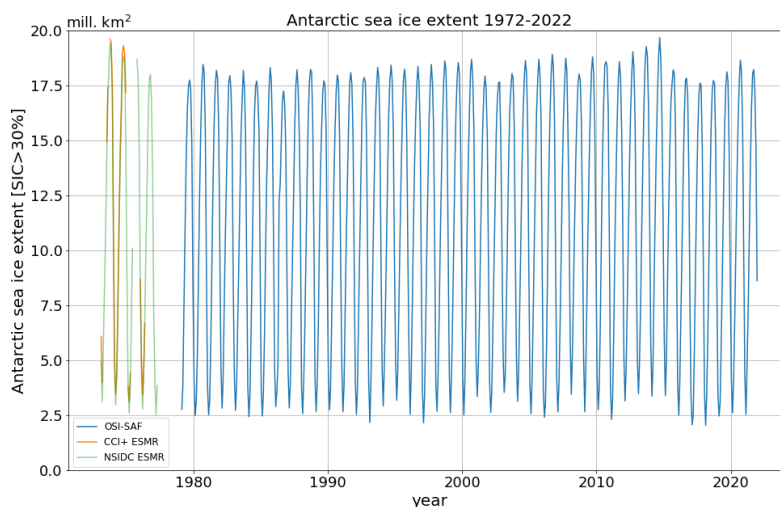


Figure 15. Monthly sea ice extent time series for the Antarctic based on a 30% sea ice threshold. The orange curve shows values of the ESMR dataset which have a 99% monthly coverage of the hemisphere, while the blue curve is based on the SIC products by OSI-SAF (EUMETSAT, 2017a & EUMETSAT, 2017b), where the 30% threshold has been applied as at: EUMETSAT, 2017c. The green line represents NSIDC's ESMR SIC product.(Parkinson et al., 2004).

5 Discussions

Comparisons between different sea ice products and the new ESMR data set proved to be more difficult than initial expected, since not only the processing algorithms differ, but also the land masks. We were not able to find two independent SIC data
295 sets for 1978 onwards and 1972-77, which share the same land mask.

Thus, it was decided at the beginning of the processing to use the same land mask as the OSI-420 product (1978 onwards) (EUMETSAT, 2020) for our ESMR data set, i.e. a 25 km equal area grid (EASE-2 version 2) land mask, to at least ensure a fair comparison between these two data sets. The NSIDC ESMR data set (green line in figures 14 & 15) used a different land mask with a polar stereographic projection (Parkinson et al., 2004), which also differs from the current NSIDC's CDR land
300 mask.

The difference in SIE is also influenced by the different projections of the data, however, the area difference between the projections is relatively small (only a few thousands of km²), so even a re-projection is expected to yield minimal differences compared to differences caused by the use of different land masks. The comparison of different land masks is complicated by the varying sea ice extent, which exposes more or less land throughout its annual cycle, and thus changes the number of
305 grid-points affected by the land mask.



The land masks land area differ between the OSI-SAF and NSIDC ESMR land mask. A comparison between the land mask land and ocean points between the NSIDC land mask and the OSI-SAF land mask showed a difference for the Northern Hemisphere of 460.000 km² (north of 60 degrees North), where the NSIDC has more land, while the difference is the opposite and much smaller in the Southern Hemisphere, with only 79.000 km² (south of 60 degrees South), where OSI-SAF's land mask has slightly more land. More land points in the land mask result in less available grid points for potential sea ice. The difference in the Southern Hemisphere sea ice extent is significantly larger and opposite to the expected contrast by the land mask difference. In the Northern Hemisphere it is not so clear how much of the SIE differences can be accounted to the land mask or algorithm differences. However, since the SIE differences are varying a lot and the differences in the Southern Hemisphere clearly cannot be explained by the land mask difference alone, it is likely that most of the SIE differences come from the algorithms and processing methods, such as the atmospheric correction and tie point calculation.

The blue curve in figures 14 & 15 is based on OSI-SAFs SIC products OSI-450 & OSI-430-b (EUMETSAT, 2017b & EUMETSAT, 2017a), corresponding to the SIE of the OSI-420 product (EUMETSAT, 2020), but instead of a 15% threshold, a 30% sea ice threshold has been used that matches the OSI-402-d sea ice extent product (EUMETSAT, 2017c).

The 30% threshold, compared to the more common 15%, was better suited for a comparison between different ESMR SIE data sets due to the relatively high noise level, which can be seen from the total uncertainty in figures 6 & 7. The uncertainty algorithm has been applied for easier data assessment and comparability to other data sets.

A large amount of ESMR data is currently filtered out, and the 99% threshold for the inclusion to the monthly timeline is especially filtering out the second half of the ESMR data, where large data gaps occurred, as seen in figure 13.

The filters worked as expected and removed erroneous T_{BS} from the raw data. To rescue more data points of the 20% of ESMR data files, that have been currently filtered out, a reprocessing of the data is planned.

To reduce the uncertainty caused by atmospheric noise, the brightness temperatures were corrected with a RTM using several atmospheric parameters from NWP (ERA-5) data, such as water vapor and wind, as input. This correction showed a consistent reduction of the standard deviation of the brightness temperatures for water points in both hemispheres, as can be seen from figures 6 & 7. Over ice surfaces the correction was less steady, since the RTM is not describing all relevant processes related to the snow and ice processes, which are the main noise source over sea ice. By correcting for atmospheric effects with ERA-5 data, we might have introduced some noise in the angular dependency for the SIC, due to the use of an incident angle dependent emissivity in the RTM (figure 1 & table 1).

To avoid biases from the RTM and the NWP data, dynamical tie points have been used, which also calibrate the algorithm to seasonal variations and instrument drift. However, we currently use mean tie-points that are independent of the incident angle. Therefore, a possible improvement for a future version of the data set might be accomplished by using angle dependent tie-points instead and this will require a complete re-calibration of the NIMBUS 5 ESMR T_B data.

Even after filtering the data for obvious errors it is clear that there are still issues with the absolute calibration of the instrument (Comiso and Zwally, 1980). For example, in 1973 after the hot-load anomaly the ocean T_B in the Southern Hemisphere is several Kelvin below the T_B level before the anomaly and in 1976 there is a dip in May and June followed by a sharp increase



340 in T_B (Zwally et al., 1983). Low frequency (timescales \geq days) T_B variations and regional variations on hemispherical scales are compensated by the dynamical SIC algorithm tie-points (Tonboe et al., 2016).

In spite of data gaps and calibration issues, the experimental NIMBUS satellite program was very successful. Applying modern processing methodologies, including dynamical tie-points and atmospheric noise reduction of the T_{BS} , reduces the noise over both ice and open water consistently. This newly processed ESMR sea ice data-set extends the existing sea ice
345 climate data record (CDR) with an important period from the 1970s. This extension of the SIE record contributes to the United Nations Sustainable Development Goals (SDGs) related to climate change by providing more observations for longer-term assessments of Arctic and Antarctic sea ice changes.

6 Conclusions

In this paper we presented a new SIC data set covering 1972-1977, by using the ESMR data from the Nimbus-5 satellite.
350 The data set consists of daily netCDF files for the Northern and Southern Hemispheres, respectively. SIC and associated uncertainties are included in the data set. The uncertainties and choice of same land mask, spatial grid and projection as for EUMETSAT's SIC CDR make comparisons between the time periods easier.

To repeat, the most important findings are:

- While the seasonal pattern is very similar to NSIDC's ESMR SIC product, our product shows systematic larger SIE
355 values, which can not be explained by differences between land masks alone. For the Northern Hemisphere our SIE values are matching the levels of the 1980s of the OSI-SAF CDR with the same land mask, while values of the Southern Hemisphere have been larger in the 1970s than in the 1980s.
- Uncertainty variables have been included in our ESMR data set for better data assessment.
- Atmospheric noise has been reduced with the use of an RTM and the ERA5 atmospheric data.
- Dynamical tie-points were used to avoid biases from the RTM and NWP data as well as to adjust to seasonal variability.
360

Data availability.

The newly processed ESMR data are released through the ESA CCI Open Data Portal:

<https://climate.esa.int/en/odp/#/project/sea-ice>

DOI: <http://dx.doi.org/10.5285/34a15b96f1134d9e95b9e486d74e49cf> (Tonboe et al., 2023)



365 **Appendix A**

A1

Table A1: The table is showing the data variables in the processing input NetCDF file and a description of each variable

Satellite variables	
Time	Time of data [year, month, day, hour, minute, second]
Brightness_temperature	Brightness temperature of the 78 scan spots [Kelvin x 10]
Latitude	latitude of the 78 scan spots [degrees x 10]
Longitude	longitude of the 78 scan spots [degrees x 10]
Pitch_fine_error	Pitch fine error [degrees x 10]
Roll_fine_error	Roll fine error [degrees x 10]
RMP_rate	RMP indicated rate high [x 10]
NADIR_LAT	Sub-satellite latitude [degrees x 10]
NADIR_LON	Sub-satellite longitude [degrees x 10]
Height	Satellite height [km]
Digital_b	A set of 1 bit status words to indicate the position of each of the command relays (users guide p. 83)
Status_indicator_1	A bit status word
Status_indicator_2	A bit status word
Data_source	A bit status word
Beam_position	A bit status word
PGM_id	Unique identification number assigned to program that prepared tapes
HOT_MEAN	Hot load mean [x 10]
HOT_RMS	RMS of hot load [x 100]
COLD_MEAN	Cold load mean [x 10]
COLD_RMS	RMS of cold load [x 100]
MUX_1	Average antenna temperature
MUX_2	Average phase shifter temperature
MUX_3	Ferrite switch temperature
MUX_4	Ambient load temperature
MUX_5	Reference load temperature
MUX_6	Automatic Gain Control
Analog_0	Analog signals (voltages)
Analog_1	Analog signals (voltages)
...	...
Analog_15	Analog signals (voltages)



ERA5 variables

u10	u component of the wind speed at 10 m (parallel to longitude) [ms^{-1}]
v10	v component of the wind speed at 10 m (parallel to longitude) [ms^{-1}]
t2m	2 m air temperature [K]
istl1	Ice internal temperature [K]
...	...
istl4	Ice internal temperature [K]
lsm	Land-sea-mask
msl	Mean sea level pressure [hPa]
siconc	Sea ice concentration [0-1]
sst	Sea surface temperature [K]
skt	Skin temperature [K]
tcw	Total column water [kgm^{-2}]
tcwv	Total column water vapor [kgm^{-2}]
era_time	Valid time for analysis

Table A2: The table shows the output variables stored in the daily NetCDF files and a description of each variable

Output variables

ice_conc	filtered sea ice concentration using atmospheric correction of brightness temperatures and open water filters [%]
raw_ice_conc_values	raw sea ice concentration estimates as retrieved by the algorithm [%]
total_standard_error	total uncertainty (one standard deviation) of sea ice concentration [%]
smearing_standard_error	smearing uncertainty of sea ice concentration [%]
algorithm_standard_error	algorithm uncertainty of sea ice concentration [%]
status_flag	status flag bits for the sea ice concentration as described in table 4
Tb_corr	corrected brightness temperatures [K]
Tb	uncorrected brightness temperatures [K]
time	Time of data [year, month, day]
xc	x coordinate of projection [km]
xy	y coordinate of projection [km]
lat	Latitude [degrees]
lon	Longitude [degrees]



Table A3. The table is showing the missing dates

Year	Missing dates											
	Jan	Feb	Mar	Apr	May	Jun	Jul	Aug	Sep	Oct	Nov	Dec
1972	-	28	1-31	1-30	1-27	-						31
1973	12-15	10-11	24-31	1-5	14-15	-						
1974	-	21	24,31	1-8,16-30	1-2	3-30						
1975	1,3,5,7, 9,13,15,17, 19,21,23,27	2,6,12, 14,16,18, 22,24,26,28	1,3,5,7,9, 11,13,15,19, 21,23,25,27,31	2,4,6,8,10, 12,14,16,18,20, 22,24,28,30	2,6,8, 10,12,20, 24,30	13,15,17, 19,21,23, 25,27,29						
1976	9-18,23, 25,27,29,31	4,6-8,10, 12,14,16,18, 20-22,24,26,28	4,6,8,10, 12,14,16,20, 26,28,30-31	1-29	1,3,5,7,9,11-16							
1977												
1972	27-28	1-31	1-4,13-16,22-23	14-15	9-10,29-30	1,5,14-17						
1973	17-19	1-8,13-14	-	22-23,25-27	1	-						
1974	1-31	1-17,19,21-25, 27,29,31	5-6,8,10, 12,14,16,18, 20,22,24, 26,28,30	2,4,6-8, 10,12,14,18, 20,22,24,26	1,3,5,7,9,11, 13,15,17,19, 21,23,25,27,29	1,3,5,7,9,11, 13,15,17,19,21, 23,25,27,29,31						
1975	1,3,5,7,9, 11,13,15,17,19,21, 23,25,27,29,31	2,4,6,8,10, 12,14,16,18,20, 22,24,26,28,30	1,5,11, 13,15,17, 23,25,27	1,3,5,7,9, 13,15,17,19,21, 23,25,27,29,31	2,4,6,8, 10,12,14,16, 18,20,22,24, 26,28,30	2,4,6,8, 10,12,14-18, 20,22,24,31						
1976												
1977												



Author contributions. WK performed the experiments, investigated the data, developed software and wrote the manuscript with contributions from all authors. RT contributed to the conceptualization, methodology, software, investigation, original draft and review & editing of the manuscript, and provided supervision throughout the work. JS contributed with critical feedback that shaped the interpretation and presentation of the data and improved the manuscript through review & editing.

370

Competing interests. The authors declare no competing interests relevant to the work presented in this paper.

Acknowledgements. This work is part of the ESA Climate Change Initiative Programme (ESA CCI) Sea Ice CCI (Sea_Ice_cci) project and the Danish National Centre for Climate Research (NCKF) at the Danish Meteorological Institute (DMI). The authors would like to thank Tadea Veng, Roberto Saldo, Thomas Lavergne, Atle Sørensen and Leif Toudal Pedersen for their inputs and valuable feedback. We would also like to thank Imke Sievers, John Andrew Dawson, and Andreas Svejgaard Jensen for developing and testing the data filters described in section 2.

375



References

- Andersen, S. & Tonboe, R. & Kern, S. & Schyberg, H.: Improved retrieval of sea ice total concentration from spaceborne passive microwave observations using Numerical Weather Prediction model fields: An intercomparison of nine algorithms. *Remote Sensing of Environment*. 380 104. 374-392. 10.1016/j.rse.2006.05.013, 2006.
- Chapman, W. L. and Walsh, J. E.: Long-range prediction of regional sea ice anomalies in the Arctic, *Weather Forecasting*, 6, 271– 288, [https://doi.org/10.1175/1520-0434\(1991\)006<0271:LRPORS>2.0.CO;2](https://doi.org/10.1175/1520-0434(1991)006<0271:LRPORS>2.0.CO;2), 1991.
- Cheon, W.G. and Gordon, A.L.: Open-ocean polynyas and deep convection in the Southern Ocean. *Sci Rep* 9, 6935, <https://doi.org/10.1038/s41598-019-43466-2>, 2019.
- 385 Comiso, J. C., and Zwally, H. J.: Correction for anomalous time dependent shifts in the brightness temperature from Nimbus 5 ESMR, NASA TM-82055, Greenbelt, Maryland, 18 pp., 1980.
- Comiso, J. C., Cavalieri, D. J., Parkinson, C. L., and Gloersen, P.: Passive microwave algorithms for sea ice concentration: A comparison of two techniques: *Remote Sensing of Environment [Remote Sens. Environ.]*, vol. 60, no. 3, pp. 357-384, Jun 1997.
- Comiso, J. C., Wadhams, P., Pedersen, L. T., and Gersten, R.A.: Seasonal and interannual variability of the Odden ice tongue and a study of 390 environmental effects. *Journal of Geophysical Research*. 106. 9093-9116. 10.1029/2000JC000204, 2001.
- EUMETSAT Ocean and Sea Ice Satellite Application Facility, Global sea ice concentration interim climate data record 2016-onwards (v2.0, 2017), OSI-430-b, (Data extracted from OSI SAF FTP server/EUMETSAT Data Center : ([2016-2022],) ([global],)) last access: 19 October 2022, 2017a.
- EUMETSAT Ocean and Sea Ice Satellite Application Facility, Global sea ice concentration climate data record 1979-2015 (v2.0, 2017), 395 OSI-450, doi: 10.15770/EUM_SAF_OSI_0008, (Data extracted from OSI SAF FTP server/EUMETSAT Data Center: ([1979-2015],) ([global],)) last access: 19 October 2022, 2017b.
- EUMETSAT Ocean and Sea Ice Satellite Application Facility, Global Sea Ice Edge product, OSI-402-d, osi-saf.eumetsat.int, last access: 19 October 2022, 2017c.
- EUMETSAT Ocean and Sea Ice Satellite Application Facility, Sea ice index 1979-onwards (v2.1, 2020), OSI-420, Data extracted from OSI 400 SAF FTP server: 1979-2019, Northern & Southern Hemisphere, last access: 19 October 2022, The OSI SAF Sea Ice Index v2.1 is made available at <https://osisaf-hl.met.no/v2p1-sea-ice-index>, 2020.
- Ferreira, D., Marshall, J., Bitz, C. M., Solomon, S., and Plumb, A.: Antarctic Ocean and Sea Ice Response to Ozone Depletion: A Two-Time-Scale Problem, *Journal of Climate*, 28(3), 1206-1226. <https://doi.org/10.1175/JCLI-D-14-00313.1>, 2015
- Fogt, R. L., Sleinkofer, A. M., Raphael, M. N., and Handcock, M. S.: A regime shift in seasonal total Antarctic sea ice in the twentieth 405 century. *Nature Climate Change* 12, 54-62, <https://doi.org/10.1038/s41558-021-01254-9>, 2022.
- Hersbach, H., Bell, B., Berrisford, P., Hirahara, S., Horányi, A., Muñoz-Sabater, J., Nicolas, J., Peubey, C., Radu, R., Schepers, D., Simmons, A., Soci, C., Abdalla, S., Abellan, X., Balsamo, G., Bechtold, P., Biavati, G., Bidlot, J., Bonavita, M., and Thépaut, J.-N.: The ERA5 global reanalysis. *Quarterly Journal of the Royal Meteorological Society*. <https://doi.org/10.1002/qj.3803>, 2020.
- Jena, B., Ravichandran, M., and Turner, J.: Recent reoccurrence of large open-ocean polynya on the Maud Rise seamount. *Geophysical 410 Research Letters*, 46, 4320– 4329. <https://doi.org/10.1029/2018GL081482>, 2019
- Kongoli, C., Boukabara, S.-A., Yan, B., Weng, F., and Ferraro, R.: A New Sea-Ice Concentration Algorithm Based on Microwave Surface Emissivities—Application to AMSU Measurements, *IEEE Transactions on Geoscience and Remote Sensing*, vol. 49, no. 1, pp. 175-189, doi: 10.1109/TGRS.2010.2052812, 2011



- Lavergne, T., Sørensen, A. M., Kern, S., Tonboe, R., Notz, D., Aaboe, S., Bell, L., Dybkjær, G., Eastwood, S., Gabarro, C., Heygster, G.,
415 Killie, M. A., Brandt Kreiner, M., Lavelle, J., Saldo, R., Sandven, S., and Pedersen, L. T.: Version 2 of the EUMETSAT OSI SAF and
ESA CCI sea-ice concentration climate data records, *The Cryosphere*, 13, 49–78, <https://doi.org/10.5194/tc-13-49-2019>, 2019.
- Markus, T., Cavalieri, D. J.: The AMSR-ENT2 sea ice concentration algorithms: its basis and implementation. *Journal of the Remote Sensing
Society of Japan* 29(1), 216-225, 2009.
- Meissner, T. and Wentz, F.: AMSR Ocean Algorithm, Algorithm Theoretical Basis Document (ATBD) Version 2,
420 <https://eosps.nasa.gov/sites/default/files/atbd/atbd-amr-ocean.pdf>, 2000.
- Meissner, T. and Wentz, F.: The emissivity of the ocean surface between 6 and 90 GHz over a large range of windspeeds and earth incidence
angles. *Ieee Transactions on Geoscience and Remote Sensing*, 50(8):3004–3026, 2012.
- NASA: The NIMBUS 5 data catalog, data orbits 8843 - 9660, volume 12, final report, 1. Oct. - 30. Nov. 1974, NASA CR 157882, 1974.
- NASA Goddard Space Flight Center (GSFC), ESMR/Nimbus-5 Level 1 Calibrated Brightness Temperature V001, Green-
425 belt, MD, USA, Goddard Earth Sciences Data and Information Services Center (GES DISC), accessed [26-06-2019],
https://disc.gsfc.nasa.gov/datacollection/ESMRN5L1_001.html, last access: 26 June 2019, 2016.
- Onarheim, I., Eldevik, T., Smedsrud, L., and Stroeve, J.C.: Seasonal and Regional Manifestation of Arctic Sea Ice Loss. *Journal of Climate*.
31. 10.1175/JCLI-D-17-0427.1, 2018.
- Parkinson, C. L., Comiso, J. C., Zwally, H. J., Cavalieri, D. J., Gloersen, P., Campbell, W. J.: Arctic sea ice, 1973-1976: satellite passive-
430 microwave observations. NASA special publications. NASA SP-489, 1987.
- Parkinson, C. L., Comiso, J. C., and Zwally, H. J., edited by Meier, W., and Stroeve, J.: Nimbus-5 ESMR Polar Gridded Sea Ice Con-
centrations, Version 1. Boulder, Colorado USA. NASA National Snow and Ice Data Center Distributed Active Archive Center. doi:
<https://doi.org/10.5067/W2PKTWMY0TP>. last access: 14 November 2022, 2004.
- Rayner, N. A., Parker, D. E., Horton, E. B., Folland, C. K., Alexander, L. V., Rowell, D. P., Kent, E. C., and Kaplan, A.: Global analyses
435 of sea surface temperature, sea ice, and night marine air temperature since the late nineteenth century, *J. Geophys. Res.*, 108, 4407,
doi:10.1029/2002JD002670, D14, 2003.
- Schanda, E.: *Physical Fundamentals of Remote Sensing*. Springer-Verlag, Berlin Heidelberg., <https://doi.org/10.1007/978-3-642-48733-0>,
1986.
- Schroeter, S., O’Kane, T., and Sandery, P.: Antarctic sea ice regime shift associated with decreasing zonal symmetry in the Southern Annular
440 Mode. <https://doi.org/10.5194/tc-17-701-2023>, 2023.
- Singh, H. A., Polvani, L. M., and Rasch, P. J.: Antarctic sea ice expansion, driven by internal variability, in the presence of increasing
atmospheric CO₂. *Geophysical Research Letters*, 46 <https://doi.org/10.1029/2019GL083758>, 2019.
- Stammerjohn, S. E., Martinson, D. G., Smith, R. C., Yuan, X., and Rind, D.: Trends in Antarctic annual sea ice retreat and ad-
vance and their relation to El Niño–Southern Oscillation and Southern Annular Mode variability, *J. Geophys. Res.*, 113, C03S90,
445 doi:10.1029/2007JC004269, 2008.
- Stroeve, J.C. and Notz, D.: Changing state of Arctic sea ice across all seasons. *Environmental Research Letters*. 13. 10.1088/1748-
9326/aade56, 2018.
- Sun, S., and Eisenman, I.: Observed Antarctic sea ice expansion reproduced in a climate model after correcting biases in sea ice drift velocity.
Nat Commun 12, 1060 (2021), <https://doi.org/10.1038/s41467-021-21412-z>, 2021.



- 450 Svendsen, E., Kloster, K., Farrelly, B., Johannessen, O. M., Johannessen, J. A., Campbell, W. J., Gloersen, P., Cavalieri, D., and Mätzler, C.: Norwegian Remote Sensing Experiment: Evaluation of the Nimbus 7 scanning multichannel microwave radiometer for sea ice research, *J. Geophys. Res.*, 88(C5), 2781– 2791, doi:10.1029/JC088iC05p02781, 1983.
- Thompson, D. W. J. and Solomon, S.: Interpretation of Recent Southern Hemisphere Climate Change, *Science*, Vol.296, 5569, p.895-899, <https://doi.org/10.1126/science.1069270>, 2002.
- 455 Titchner, H. A., and Rayner, N. A.: The Met Office Hadley Centre sea ice and sea surface temperature data set, version 2: 1. Sea ice concentrations, *J. Geophys. Res. Atmos.*, 119, 2864– 2889, doi:10.1002/2013JD020316, 2014.
- Tonboe, R. T.: The simulated sea ice thermal microwave emission at window and sounding frequencies. *Tellus A*, 62(3):333–344, 2010.
- Tonboe, R. T., Eastwood, S., Lavergne, T., Sørensen, A. M., Rathmann, N., Dybkjær, G., Pedersen, L. T., Høyer, J. L., and Kern, S.: The EUMETSAT sea ice concentration climate data record, *The Cryosphere*, 10, 2275–2290, <https://doi.org/10.5194/tc-10-2275-2016>, 2016.
- 460 Tonboe, R., Nandan, V., Mäkynen, M., Pedersen, L., Kern, S., Lavergne, T., Øelund, J., Dybkjær, G., Saldo, R., and Huntemann, M.: Simulated Geophysical Noise in Sea Ice Concentration Estimates of Open Water and Snow-Covered Sea Ice. *IEEE Journal of Selected Topics in Applied Earth Observations and Remote Sensing*. PP. 1-1. 10.1109/JSTARS.2021.3134021, 2021.
- Tonboe, R.T., Kolbe, W.M., Toudal Pedersen, L., Lavergne, T., Sørensen, A., and Saldo, R.: ESA Sea Ice Climate Change Initiative (Sea_Ice_cci): Nimbus-5 ESMR Sea Ice Concentration, version 1.0. NERC EDS Centre for Environmental Data Analysis, 03 February 2023. doi:10.5285/34a15b96f1134d9e95b9e486d74e49cf. <http://dx.doi.org/10.5285/34a15b96f1134d9e95b9e486d74e49cf>, 2023.
- 465 Turner, J., Comiso, J. C., Marshall, G. J., Lachlan-Cope, T. A., Bracegirdle, T., Maksym, T., Meredith, M. P., Wang, Z., and Orr, A.: Non-annular atmospheric circulation change induced by stratospheric ozone depletion and its role in the recent increase of Antarctic sea ice extent, *Geophys. Res. Lett.*, 36, L08502, doi:10.1029/2009GL037524, 2009.
- Ulaby, F. T., Moore, M. K., and Fung, A. K.: *Microwave Remote Sensing, Active and Passive*, Vol. 3, Artech House, Norwood, MA, 1986.
- 470 Veng, T.: Mapping of sea ice using NIMBUS 5 ESMR satellite data. Master thesis. DTU Space. 2021. <https://findit.dtu.dk/en/catalog/6059da9cd9001d016554ff7a>, 2021.
- Walsh, J. E., Fetterer, F., Stewart, J. S., and Chapman, W. L.: A database for depicting Arctic sea ice variations back to 1850, *Geographical Review*, 107:1, 89-107, DOI: 10.1111/j.1931-0846.2016.12195.x, 2017.
- Walsh, J. E., Chapman, W. L., Fetterer, F., and Stewart, J. S.: Gridded Monthly Sea Ice Extent and Concentration, 1850 Onward, Version 2 [Data Set]. Boulder, Colorado USA. National Snow and Ice Data Center. <https://doi.org/10.7265/jj4s-tq79>. Last Access: 14 November 2022, 2019.
- 475 Wang, G., Hendon, H. H., Arblaster, J.M. et al.: Compounding tropical and stratospheric forcing of the record low Antarctic sea-ice in 2016. *Nat Commun* 10, 13 (2019). <https://doi.org/10.1038/s41467-018-07689-7>, 2019.
- Wentz, F. J.: A model function for ocean microwave brightness temperatures, *J. Geophys. Res.*, 88(C3), 1892– 1908, doi:10.1029/JC088iC03p01892, 1983,
- 480 Wentz, F. J.: A well-calibrated ocean algorithm for special sensor microwave / imager, *J. Geophys. Res.*, 102(C4), 8703– 8718, doi:10.1029/96JC01751, 1997
- Zwally, H. J., Comiso, J. C., Parkinson, C.L., Campbell, W. J., Carsey, F. D., and Gloersen, P.: Antarctic sea ice 1973-1976: Satellite passive microwave observations. NASA SP-459, Washington DC, pp. 206, 1983.